

Nitrogen/Phosphorus Dual-Doped Hard Carbon Anode with High Initial Coulombic Efficiency for Superior Sodium Storage

Sheng Wu,^[a] Xiaoyi Lu,^[a] Kaili Zhang,^[b] Junling Xu,*^[a] and Zhipeng Sun*^[a]

Among anode materials for sodium-ion batteries (SIBs), hard carbon (HC) gains more attention due to its low cost, high electronic conductivity, and renewable resources. However, sluggish kinetics result in its low-rate capability and unfavorable cycle stability. Moreover, HC often presents low initial Coulombic efficiency (ICE), which also limits the utilization of the battery capacity and energy density. Herein, nitrogen and phosphorus dual-doped HC (denoted as NPHC) with network structure is synthesized by a facile interfacial polymerization method, which endows the NPHC with synergistic effects of the enlarged interlayer spacing and improved conductivity. Con-

sequently, the obtained NPHC exhibits a high reversible capacity (286 mAh g^{-1} at 0.1 A g^{-1}), excellent rate capability (144 mAh g^{-1} at 10 A g^{-1}), high ICE (71%), and remarkable cyclability over 2000 cycles at 1 A g^{-1} . Moreover, the storage mechanism of sodium ions is examined by a series of *ex-situ* characterizations. Additionally, when coupled with $\text{Na}_3\text{V}_2(\text{PO}_4)_2\text{F}_3$ as a cathode, the full cell delivers superior cyclability (capacity retains 90% over 300 cycles at 1 A g^{-1}). This work may shed new insight into designing other carbon-based electrode materials for high-performance energy storage.

Introduction

Sodium-ion batteries (SIBs) have attracted extensive attention owing to rich resources, low cost, and competitive performance.^[1–4] Numerous anode materials have been well explored for SIBs, for example, carbon materials,^[5–7] metal oxides,^[8–10] metal sulfides,^[11] metal selenides,^[12] and alloys.^[13] Among these, carbon materials, especially hard carbon, have been considered the best option for sodium-ion storage due to their high electronic conductivity, renewable resources, and low cost.^[14,15] Moreover, the hard carbon shows to be more suitable for sodium ion (Na^+) insertion. However, SIBs based on hard carbon often exhibit sluggish kinetics because of the larger radius of Na^+ , leading to low-rate capability and unfavorable cycle stability. Moreover, hard carbon always presents low initial coulombic efficiency (ICE), which also limits the utilization of the battery capacity and energy density.

In order to solve these problems, researchers have come up with many solutions, such as low-temperature carbonization, heteroatom doping, and the creation of closed nanopores.^[16] As reported, heteroatom doping is regarded as one of the fastest and most effective methods to boost the rate capability

and cycle stability, because it can enhance the capacitive behavior and enlarge the layer spacing to improve the diffusion kinetics.^[17–20] As N-doping can significantly improve electrical conductivity, the nitrogen atom has been well-studied as one of the most widely used heteroatoms. Besides, the introduction of pyridinic and pyrrolic nitrogen can also promote sodium storage ability by efficiently producing defects and active sites.^[21,22] For example, the reversible capacity of biomass-derived hard carbon material increased significantly from 196 to 231 mAh g^{-1} at 0.2 A g^{-1} by adopting an N-doping strategy.^[23] Except for N-doping, P and S doping can also lead to highly distorted carbon structures and larger layer spacing due to their large ionic radius and weak electronegativity.^[24,25] Therefore, heteroatom doping is often used as a way “to kill two birds with one stone”, the synergistic effect of double doping is widely used to improve the capacity of carbon materials. Li et al. prepared an N/P dual-doped graphene sheet, which can deliver a capacity of 189 mAh g^{-1} at 3 A g^{-1} .^[26] Another N, P co-doped porous carbon prepared by Zhou et al. remained 140 mAh g^{-1} at 10 A g^{-1} .^[27] However, high heteroatom doping can introduce excessive defects resulting in a low ICE. At the same time, with hard carbon containing a large number of irregular graphite microcrystals and structural micro-pores, hard carbon is usually accompanied by a larger specific surface area, which is the main factor affecting ICE. It is generally accepted that hard carbon materials with a high surface area are often accompanied by low ICE. In addition, Luo et al.^[28] reported that if GO was added to sucrose before carbonization, the surface area of the prepared hard carbon could be effectively limited to only $5.4 \text{ m}^2 \text{ g}^{-1}$ compared with $137.2 \text{ m}^2 \text{ g}^{-1}$ for materials prepared without GO. Therefore, ICE with a low specific surface area of hard carbon can be increased from 74% to 83%. As a result, it is possible to obtain excellent

[a] S. Wu, X. Lu, Dr. J. Xu, Prof. Dr. Z. Sun
School of Materials and Energy
Guangdong University of Technology
Guangzhou, 510006, Guangdong, China
E-mail: jlxu@gdut.edu.cn
zpsunxj@gdut.edu.cn

[b] Prof. K. Zhang
Department of Mechanical Engineering
City University of Hong Kong
83 Tat Chee Avenue, Hong Kong, China

 Supporting information for this article is available on the WWW under
<https://doi.org/10.1002/batt.202200427>

performance and high ICE by appropriately reducing the specific surface area with guaranteed performance. But the relationship between heteroatom doping and ICE has to be further investigated.

In this work, we successfully prepared one kind of N/P-rich hard carbon material (NPHC), which greatly improved sodium storage capability as the anode for SIBs. Compared with single atomic doping, dual-doped NPHC shows larger layer spacing (0.421 nm) and more defect levels, leading to an excellent rate performance (286 and 144 mAh g⁻¹ at 0.1 and 10 Ag⁻¹, respectively) and better cycle performance (the reversible capacity remains 183 mAh g⁻¹ at 1 Ag⁻¹ over 2000 cycles), this verifies the synergistic effect of N/P dual-doping on improving the storage capacity of sodium. Our prepared NPHC also delivers a relatively high ICE (71%) benefiting from its low specific surface area (11.3 m² g⁻¹). By combining the Na₃V₂(PO₄)₂F₃ cathode, the full battery shows a high capacity of 160 mAh g⁻¹ at 0.1 Ag⁻¹ and a good long lifetime (capacity retains 90% over 300 cycles at 1 Ag⁻¹). Our study can not only improve the storing capacity of the sodium by dual-doping but also open up a new way for the study of hard carbon as SIBs anode materials.

Results and Discussion

N/P dual-doped hard carbon (NPHC) precursor used a simple polymerization method to prepare as shown in the scheme of Figure 1. With the contact between two immiscible solutions, the aniline and phytic acid occurred cross-linking reactions at the interface between the two liquid phases. As the dopants and cross-linking agents, phytic acid can not only introduce phosphorus atoms but also promote the formation of cross-linking structures. In the continuous reaction, a green gel-state precursor appeared and grew thick until the reactants were exhausted. As the reaction occurs in the middle of solutions, the organic species can protect the formation of free radicals and avoid side reactions by isolating oxygen during the process

of reaction. After a pyrolysis process under an inert atmosphere, the obtained green organic matter can be carbonized to the finally NPHC samples.

The morphology of NPHC was characterized as shown in Figure 2(a). It is obvious that a plentiful interpenetrating network is formed with a high degree of cross-linking (Figure 2b). Polyaniline (NHC) forms a fibrous structure (Figures S1a and b, Supporting Information) without phytic acid. As shown in Figures 2(c) and S1(c) (Supporting Information), both NPHC and NHC are amorphous states with some microcrystalline regions. The layered spacing of NPHC is about 0.46 nm, which is much larger than that of NHC (0.34 nm), which can be attributed to P-doping inducing the increase of layered spacing. The elemental mapping (Figure 2d) shows C, N, O, and P are evenly distributed among NPHC, indicating our success of the N/P dual-doping strategy. The elemental mapping analysis of NHC is shown in Figure S1(d), also indicating a successful introduction of N to NHC.

Figure 3(a) shows the X-Ray diffraction (XRD) characterizations. A wide diffraction peak of NHC appeared at around 24°, which refers to (002) planes.^[29] For comparison, the peak (002) of NPHC shifts to a lower angle (21.5°) than NHC. According to the Bragg equation, the interlayer distance of NPHC is 0.421 nm and NHC is 0.372 nm, which is consistent with the result of the high-resolution transmission electron microscopy (HR-TEM) images. This indicated that P-doping could enlarge the layered space of hard carbon. Raman spectra (Figure 3b) show two peaks at 1340 cm⁻¹ (the D band related to defects) and 1585 cm⁻¹ (the G band related to sp²-carbon).^[30] The defect content can be obtained by calculating the I_D/I_G ratio. We calculated that the I_D/I_G of NHC is 0.91, while NPHC exhibits a higher I_D/I_G ratio of 1.07, indicating that P-doping can introduce more defects, which also means more active sites for sodium-ion storage.

We further used X-ray photoelectron spectroscopy (XPS) to analyze the chemical valence states of NPHC and NHC as shown in Figure 3(c). There is no presence of P element detected in NHC, the same as the previous results of the

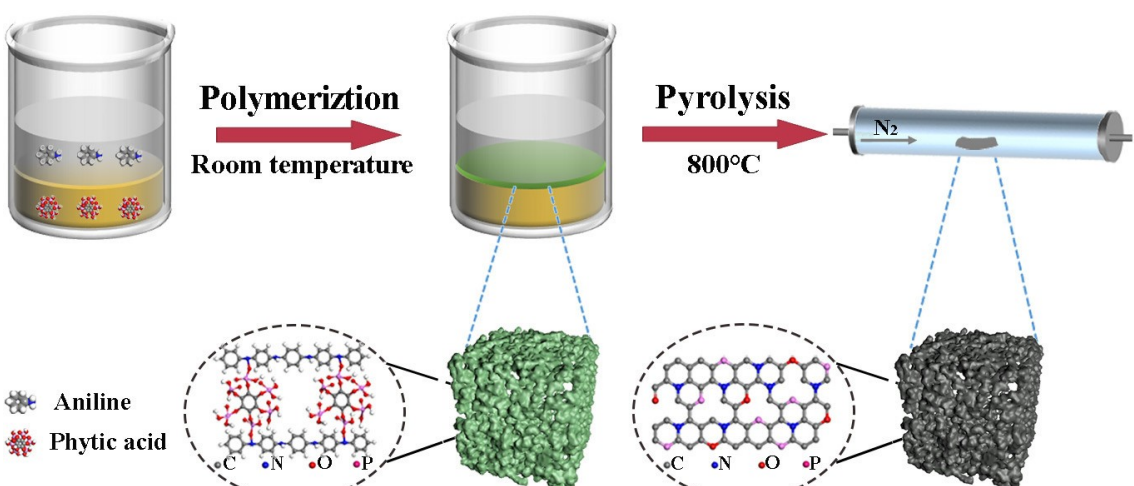


Figure 1. Diagram of the synthesis process for NPHC.

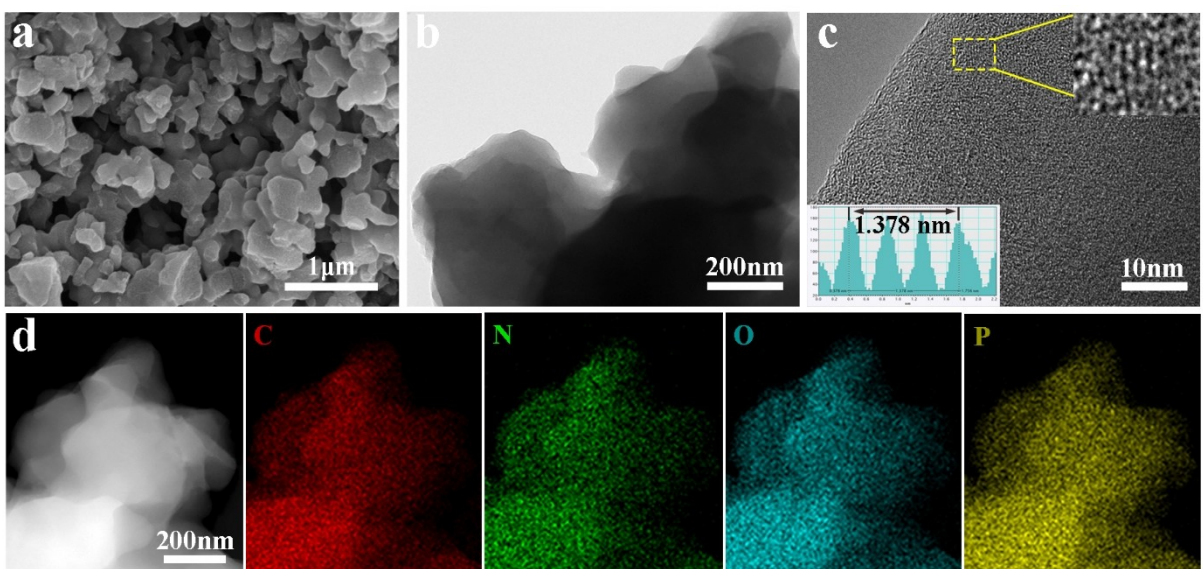


Figure 2. Morphologies of prepared NPHC. a) SEM image, b) TEM image, and c) HR-TEM image of NPHC (inset: lattice fringes of NPHC and its corresponding interlayer distances). d) HAADF-STEM and corresponding elemental mapping images of NPHC.

energy-dispersive X-ray spectroscopy (EDS). Four elements including C, N, O, and P are investigated in detail. The high-resolution spectrum of C 1s (Figure 3d) shows three peaks at 284.7, 286.0, and 288.6 eV are connected with C—C/C=C, C—N/C—P, and C=O, respectively.^[31] As shown in Figure 3(e), the N 1s high-resolution spectrum can be made up of pyridinic-N (398.7 eV), pyrrolic-N (400.8 eV), graphitic-N (402.6 eV), and oxidized-N (404.3 eV).^[32,33] The high-resolution spectrum of O 1s (Figure 3f) can be divided into C=O, C—O, and O—C=O.^[34] Meanwhile, Figure 3(g) shows the peak of P 2p spectrum at 133.0 eV is P—C, which reveals that the P doping achieved by this method is bonded by a chemical bond. The P—O bond located at 134.0 eV may be associated with oxidation by contact with air.^[35,36] Table S1 (Supporting Information) summarizes contents of different elements of both NHC and NPHC. NPHC demonstrates a high N content of 6.99% and P content of 4.7% and it can be found that contents of pyridinic-N (3.10%) and pyrrolic-N (2.53%) in NPHC are much higher than those in NHC (pyridinic-N 2.81%, pyrrolic-N 1.33%). Pyridinic-N and pyrrolic-N play an extremely key role in the storage process of sodium ions, which can introduce abundant edge defects and active sites for the rapid kinetics of sodium ion storage. N₂ adsorption and desorption isotherm measurement was used to acquire the porosity and Brunauer-Emmett-Teller (BET) surface area. Figure 3(h and i) shows that NPHC has a lower specific surface area ($11.3 \text{ m}^2 \text{ g}^{-1}$) than NHC ($316.8 \text{ m}^2 \text{ g}^{-1}$), the decrease of the specific surface area should be caused by the greater cross-linking degree that results in less internal pore structure which leads to the low specific surface area. Low surface area is the key for NPHC to achieve high ICE because the low surface area can effectively reduce the generation of irreversible reactions in the first cycle. However, the average pore diameter of NPHC is 11.9 nm, which is much larger than that of NHC (4.8 nm).

The electrochemical behavior was measured by the cyclic voltammetry (CV) technique. Figure 4(a) shows the CV curve of NPHC at 0.1 mV s^{-1} . A wide irreversible peak appears at about 0.75 V, which is related to the formation of a solid electrolyte interface (SEI) film in the first cycle.^[37,38] A pair of sharp redox peaks appear at a low potential (0–0.1 V), which is due to sodium-ion insertion/desertion between graphite layers.^[39] The CV curve at 0.1 mV s^{-1} of NHC is shown in Figure S2 (Supporting Information), and an irreversible peak also appears at about 0.75 V. However, there is no obvious redox peak at the low potential range, indicating that there is no intercalation of sodium ions in NHC, which is consisted of the absence of plateau region in the charge-discharge curves (Figure S3, Supporting Information). We suspect that the plateau region of sodium ions in NPHC is more likely caused by the intercalation behavior because the P-doping expands layer spacing is feasible to accommodate sodium ions. In the last two cycles, the CV curves of NPHC and NHC show high coincidence, indicating good reversibility during the cycle. As shown in the first three charge and discharge cycles of NPHC at 0.1 A g^{-1} (Figure 4b), the reversible capacity reaches 309 mAh g^{-1} , much higher than 159 mAh g^{-1} of NHC (Figure S3, Supporting Information). Moreover, both NPHC and NHC have relatively high initial coulombic efficiency (ICE) compared to most hard carbon anodes,^[40–42] and the ICE of NPHC (71%) is higher than that of NHC (67%). The ICE cannot reach 100% because the irreversible capacity is lost due to the formation of SEI film, which is the same as the CV curve. Figure 4(c) shows the cyclic performance of NPHC and NHC at 0.1 A g^{-1} . NPHC delivers a capacity of 255 mAh g^{-1} with a low decay rate of only 0.11% for each cycle, indicating that NPHC has excellent cyclic stability. The reversible capacity of NHC after 100 cycles retains 159 mAh g^{-1} . The rate capacities of NPHC and NHC are shown in Figure 4(d). NPHC shows a much better rate performance,

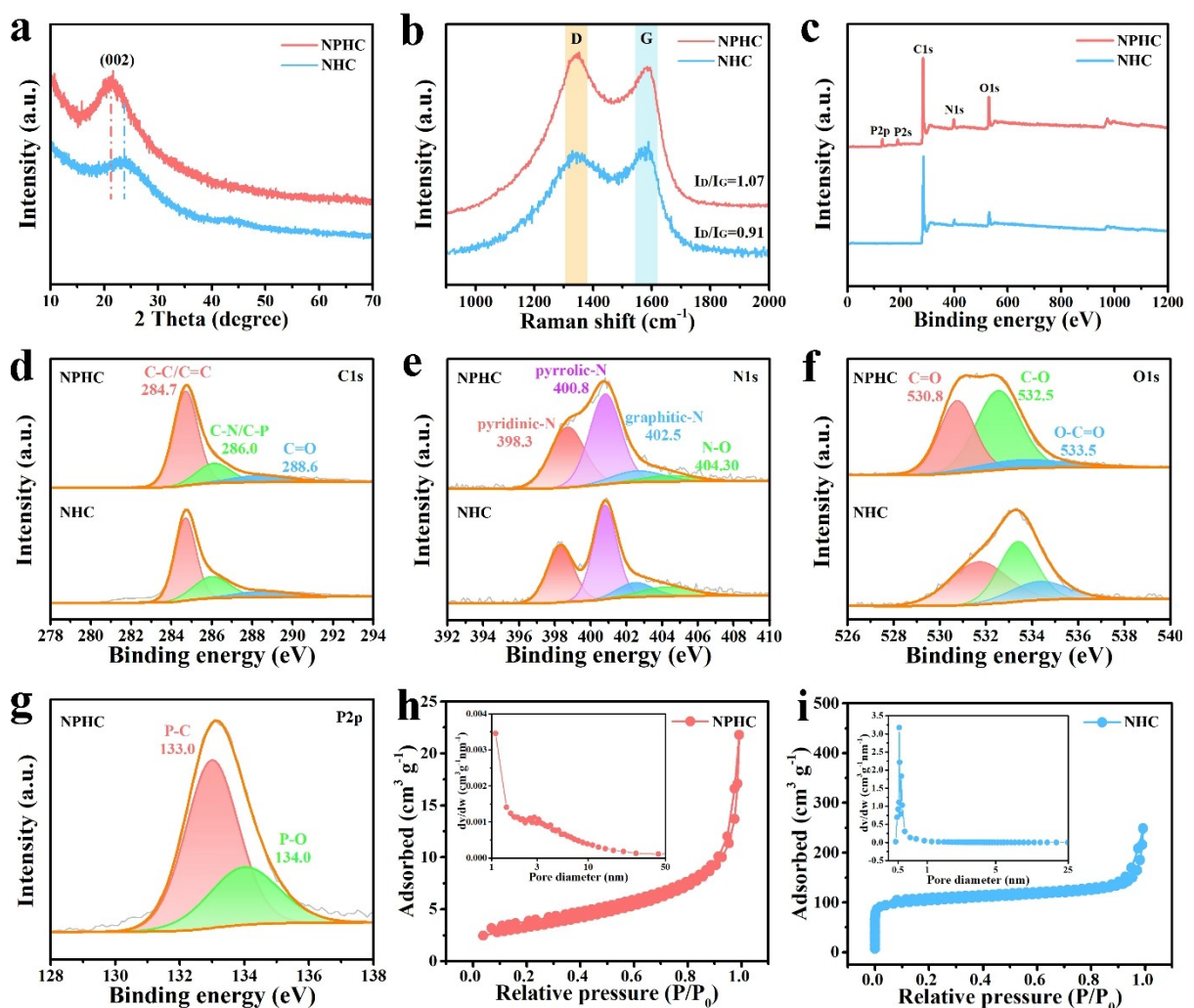


Figure 3. Spectra of prepared hard carbons. a) XRD patterns, b) Raman spectrum, and c) XPS spectra of NPHC and NHC. d) C 1s, e) N 1s, and f) O 1s spectra of NPHC and NHC. g) P 2p spectra of NPHC. h, i) N_2 adsorption/desorption isotherms and pore diameter distribution of NPHC and NHC, respectively.

the reversible capacities of 286, 262, 239, 221, 200, and 169 mAh g^{-1} are gained at 0.1, 0.2, 0.5, 1, 2, and 5 Ag^{-1} , respectively. Even at 10 Ag^{-1} , it can still hold 144 mAh g^{-1} . For comparison, NHC is only 66 mAh g^{-1} at 10 Ag^{-1} . What is noteworthy is that capacity is back to 275 mAh g^{-1} when the current density restores to 0.1 Ag^{-1} , indicating that NPHC has good reversibility and excellent structural stability. Our NPHC shows a more excellent rate performance than the previously reported hard carbon materials, especially at high current density (Figure 4e).^[24,27,42–46] Moreover, we also investigate the influences of PA concentrations and carbonization temperatures on the rate performance of samples (Figures S4a and b, Supporting Information). Our NPHC anode (PA was 2 mL and carbonization temperature was 800 °C) shows the best rate performance. The long-life cyclic performance of NPHC under 1 Ag^{-1} is illustrated in Figure 4(g). The capacity remains at 183 mAh g^{-1} and decreases by 0.8% per cycle after 2000 cycles, demonstrating significant long-term cyclic stability. However, the capacity of NHC is only 134 mAh g^{-1} after 2000 cycles at 1 Ag^{-1} . In addition, NPHC shows a high capacity of 152 mAh g^{-1}

at 5 Ag^{-1} after 1300 cycles (Figure S5, Supporting Information), indicating that NPHC has excellent cyclic stability even at a high rate. The electrical resistances for NHC and NPHC were analyzed by electrochemical impedance spectroscopy (EIS) that used a 10 mV alternating current signal with a frequency from 0.01 to 100 kHz. All samples are made up of semicircles and oblique lines (Figure 4f). Through equivalent circuit fitting of the obtained data, values of equivalent series resistance R_s (mainly related to electrolyte resistance) and charge transfer resistance R_{ct} could be obtained.^[47] It can be found that the semicircle diameter of NPHC is smaller than that of NHC, indicating that the charge transfer resistance decreases and the electron transfer speed increases after N/P dual-doping.

The sodium storage properties of carbon materials depend on such factors as their electrical conductivity, specific surface area, and defect content. Compared with NPHC, NHC has a higher specific surface area, which leads to a large amount of irreversible consumption of sodium ions during the formation of SEI, resulting in a relatively low capacity. However, NPHC has high defect content and electrical conductivity. Combining

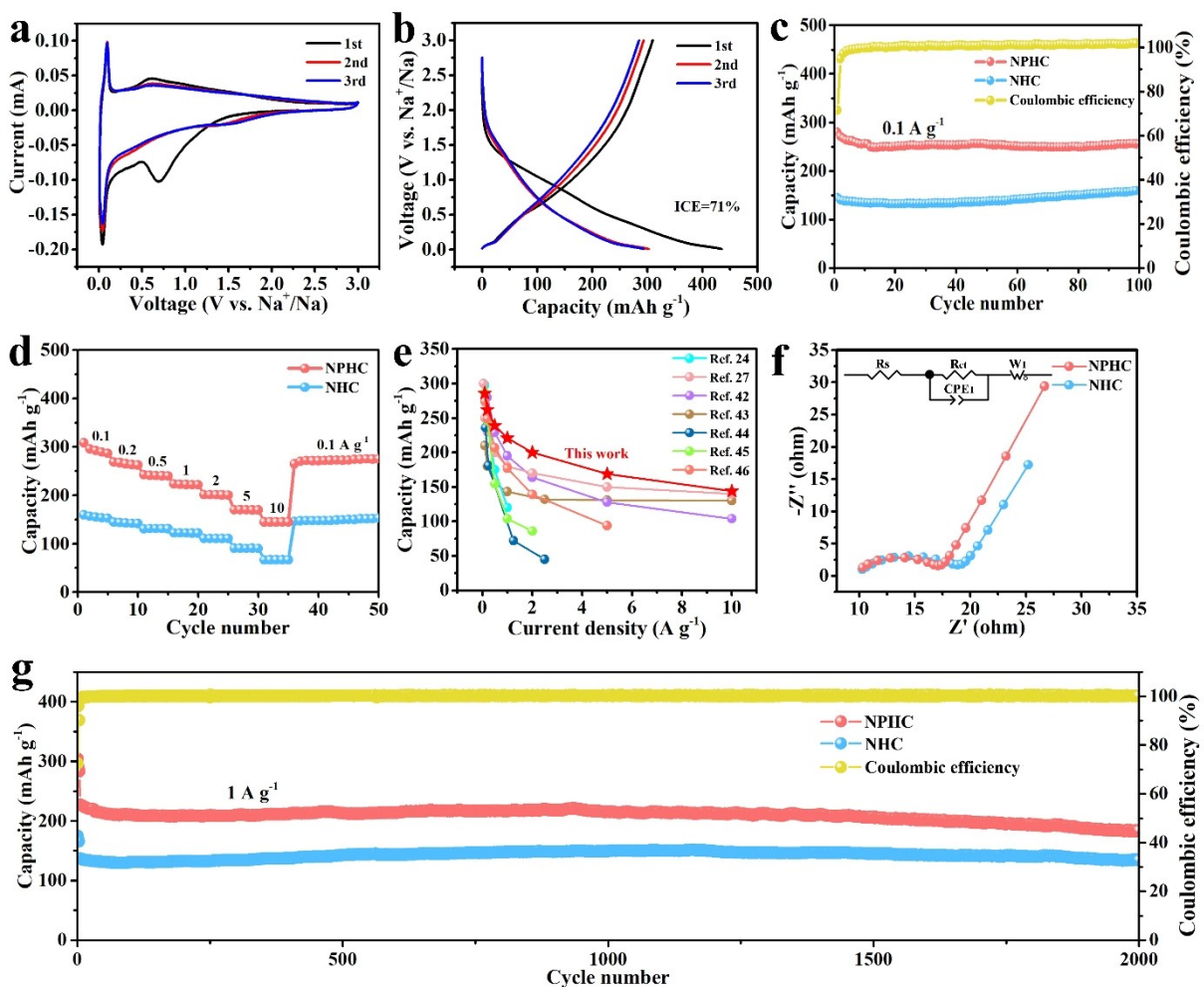


Figure 4. Battery performances of prepared hard carbons. a) CV curves of NPHC at 0.1 mVs^{-1} . b) The charge and discharge curves at 0.1 A g^{-1} of NPHC. c) Cyclic performance at 0.1 A g^{-1} and d) rate capability for NPHC and NHC. e) Comparisons of rate performances. f) The electrochemical impedance spectra and g) long-life cyclic performance at 1 A g^{-1} for NPHC and NHC.

these two factors, NPHC has good cycling stability, rate performance, and reversibility.

To study the sodium storage mechanism and kinetic behavior of the NPHC electrode, CV curves ranging from $0.1\text{--}5 \text{ mVs}^{-1}$ were evaluated (Figure 5a). The peak positions did not change largely with scan rates increasing, indicating a small polarization at different scan speeds. The relationship between peak currents and sweep speeds is as follows in Equation (1).^[48,49]

$$i = av^b \quad (1)$$

Here, a and b are certain. The b value can be calculated by the graph of $\log(i)$ and $\log(v)$. When the b value is 1, indicating the surface capacitance controls the process. If the b value equals 0.5, meaning diffusion controls the sodium storage process. The calculated b value for NPHC is 0.86 (Figure 5b), indicating the storage of sodium ions is controlled by these two behaviors.^[50]

The mechanism of sodium-ion storage was further studied by the *ex-situ* Raman spectrum. As shown in Figure 5(c), in

discharge process, the G-peak of Raman spectrum shifts to a low wavenumber, corresponding to the insertion of sodium ions, and the G peak moves to the initial location with the desorption of sodium ions.^[51] Meanwhile, the I_D/I_G ratios corresponding to each charge/discharge of states are calculated and summarized as shown in Figure 5(c). During discharge process, the I_D/I_G value decreases from 1.07 to 1.02, indicating that the defect sites are reducing, which may be caused by the filling effect of sodium ions on the defect sites. Besides, it is noted that the I_D/I_G value increases and gradually returns to the initial value during charging to 3.0 V with the sodium ion released at the defect location. It shows that NPHC has satisfactory reversibility in the whole process, which further confirms that NPHC has excellent structural stability. In addition, the diffusion behavior in NPHC and NHC was measured by galvanostatic intermittent titration technique (GITT) at 0.1 A g^{-1} with a pulse current interval of 10 minutes and rest for 1 h. Figure S6 (Supporting Information) shows GITT curves of NPHC and NHC. Diffusion coefficients can be got as the following formula.

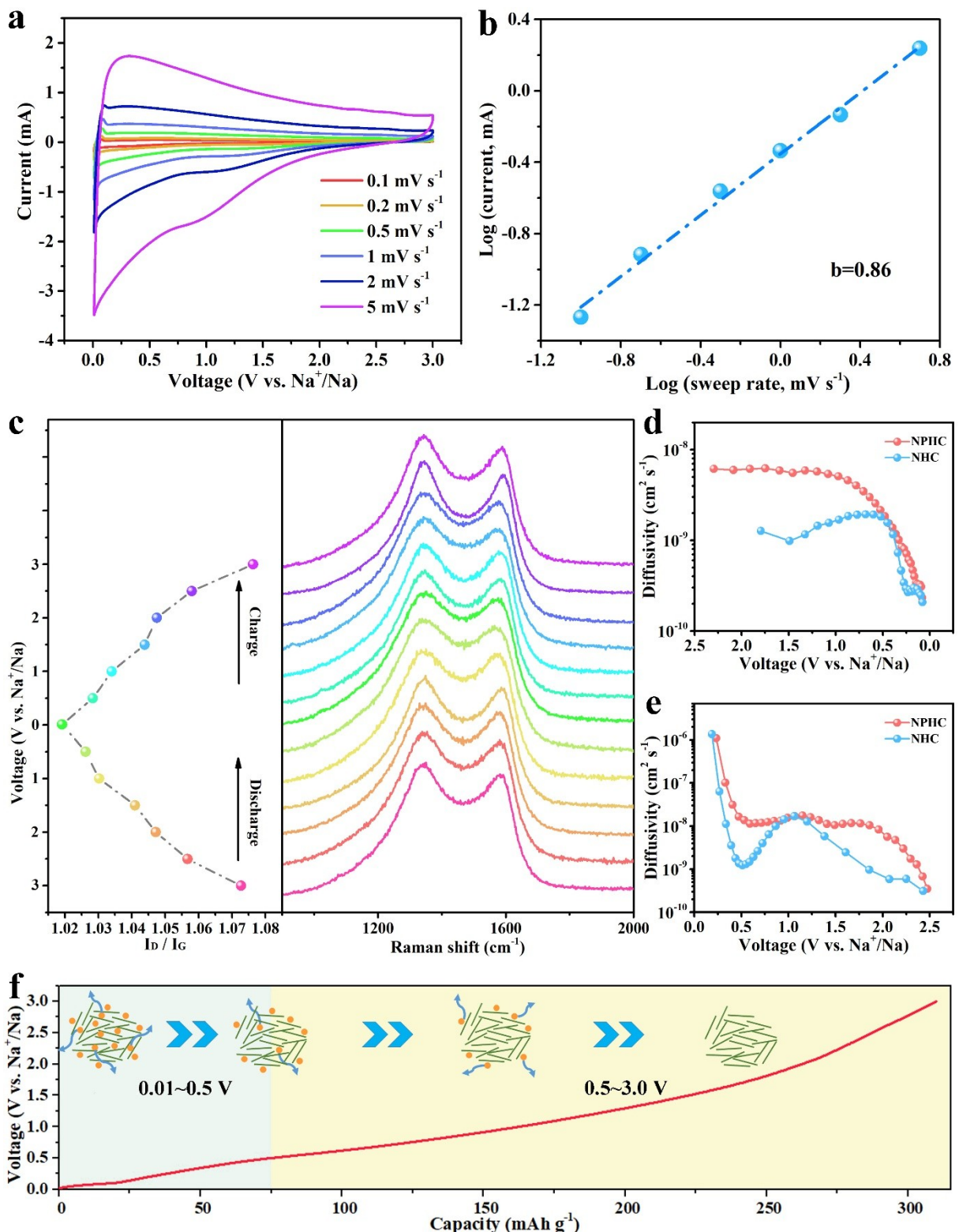


Figure 5. Electrochemistry of prepared hard carbons. a) CV curves of NPHC at scan rates (0.1–5 mVs⁻¹). b) Plots of log(scan rate) versus log(peak current), calculated from CV curves. c) Ex-situ Raman spectrum of NPHC and calculated I_D/I_G ratios. d, e) The calculated diffusion coefficients of NPHC and NHC at 0.05 Ag⁻¹. f) Schematic illustration of the sodium ion storage process in charging.

$$D = \frac{4}{\pi \tau} \left(\frac{m_B V_M}{M_B S} \right)^2 \left(\frac{\Delta E_S}{\Delta E_\tau} \right)^2 \quad (2)$$

where τ is the pulse duration; m_B is the mass of the electrode material; V_M is the molar volume of the electrode material; M_B is the molar mass of the electrode; S is the area of the electrode;

ΔE_s is the voltage change caused by pulse; ΔE_t is the voltage change of constant current charge (discharge). In the discharge process, the diffusion coefficient of sodium ions in NPHC keeps decreasing with the potential close to 0 V (Figure 5d), while the diffusion coefficient of NHC shows the same situation. The diffusion coefficient in the charging process shows an opposite trend (Figure 5e), which further demonstrates the reversibility of sodium ions in the diffusion process. But in the whole process, the diffusion coefficient of sodium ion in NPHC (an average of $10^{-8} \text{ cm}^2 \text{s}^{-1}$) is larger than that in NHC ($10^{-9} \text{ cm}^2 \text{s}^{-1}$), which indicates that the introduction of abundant defect sites after P doping can promote the rapid diffusion of sodium ion. The ex-situ Raman spectroscopy and GITT curves can also reveal the sodium ion storage mechanism (Figure 5f). During the discharge process, the adsorption of sodium ions in the sloping region leads to the reduction of defect level and a faster ion diffusion rate. From 0.5 V to 0.1 V, it can be regarded as sodium ions are adsorbed in the nanopore, but the rate of ion diffusion decreases. Different from the adsorption reaction in the sloping region, the intercalation behavior of sodium ions in the plateau region (0.1–0 V) is relatively slow because the ion diffusion resistance is large, which is similar to the intercalation

behavior of Li ions in graphite. In the following charging process (0–3.0 V), the sodium ions on the surface and between the layers of NPHC gradually emerge and return to the initial state. Therefore, it can be concluded that the adsorption and intercalation mechanism of sodium ions in hard carbon.^[52]

To further investigate the practical application value of NPHC anode, $\text{Na}_3\text{V}_2(\text{PO}_4)_2\text{F}_3$ (NVPF) cathode material was combined with NPHC to assemble a full battery (Figure 6a). NVPF cathode material was synthesized by microwave hydrothermal method as previously reported,^[53,54] and its XRD patterns were shown in Figure S7 (Supporting Information). To further improve the coulombic efficiency, both NVPF and NPHC were activated five cycles in sodium-ion half batteries at 0.1 A g^{-1} . Figure 6(b) shows the charge/discharge curves at 0.1 A g^{-1} , the reversible capacity stabilizes at 160 mAh g^{-1} after 10 cycles. As shown in Figure 6(c), discharge capacities of the full battery are 163, 145, 104, 65, and 39 mAh g^{-1} at 0.1 – 2.0 A g^{-1} , respectively. When returning to 0.1 A g^{-1} , it gets back to 160 mAh g^{-1} . In addition, NVPF//NPHC full battery also shows excellent cycling stability, which can achieve a reversible capacity of 160 mAh g^{-1} after 100 cycles (Figure 6d) and 81 mAh g^{-1} after 300 cycles (Figure 6e) at 0.1 and 1 A g^{-1} ,

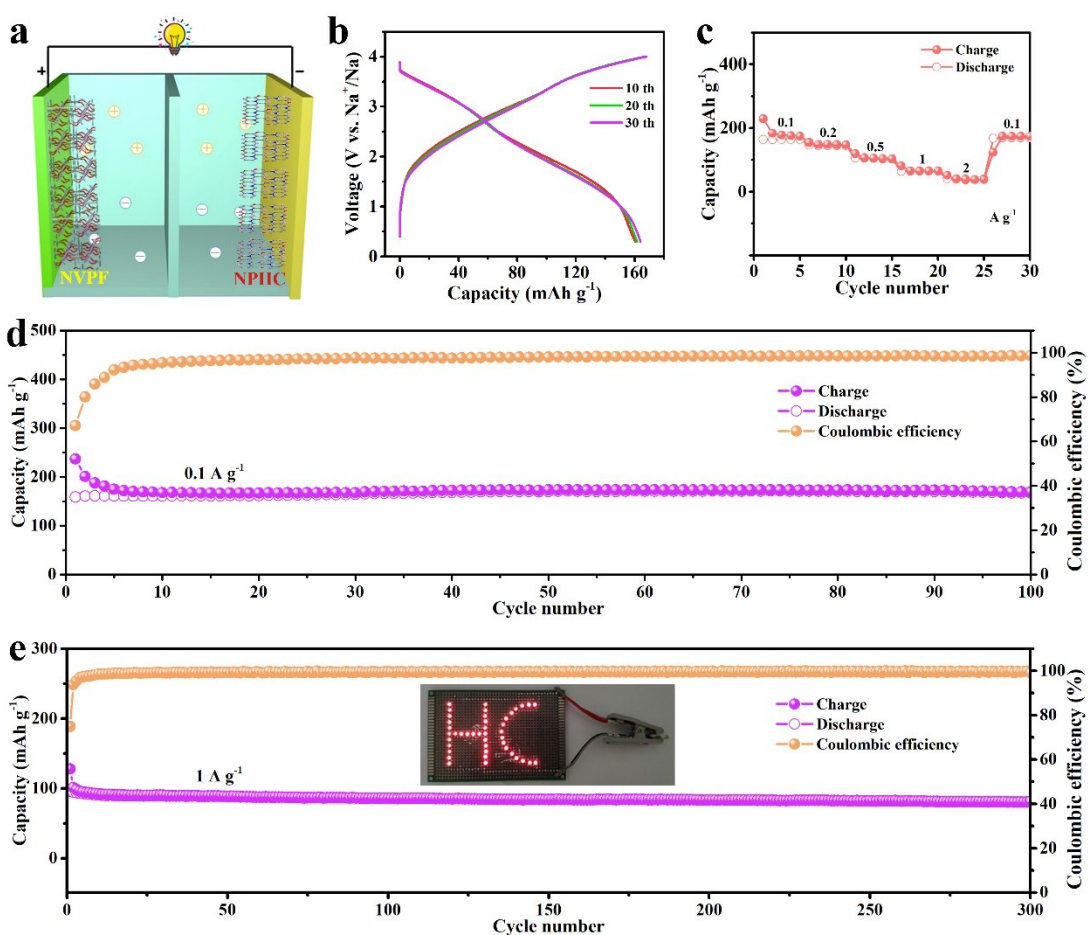


Figure 6. Na-ion full batteries with prepared hard carbon as an anode. a) Schematic illustration of the sodium-ion full battery. b) Charge/discharge curves at 0.1 A g^{-1} from 0.3 V to 4.0 V. c) The rate capability at the current densities of 0.1 – 2 A g^{-1} . d, e) The cyclic performance of the full battery at 0.1 A g^{-1} and 1 A g^{-1} , respectively (inset: 43 LEDs powered by the full battery).

respectively. And a coulombic efficiency keeps around 100%. The relation between energy density and power density is obtained from the total mass of cathode and anode active materials (Figure S8, Supporting Information), the full battery can reach the energy density of 115 Wh kg^{-1} at a power density of 70 W kg^{-1} , and a power density of 508 W kg^{-1} with an energy density of 10 Wh kg^{-1} . Our assembled NVPF//NPHC full battery can light 43 LED bulbs together as shown in the inset, which further exhibits its potential worth in practical applications.

Conclusion

In summary, an interpenetrating network of hard carbon with N/P dual-doped (NPHC) is prepared by a facile interfacial polymerization method. Due to the improved conductivity and expanded layer spacing, NPHC shows superb rate capability and long cyclic stability. Specifically, the reversible capacity of 286 and 144 mAh g^{-1} at 0.1 and 10 A g^{-1} , respectively, and the reversible capacity remains 183 mAh g^{-1} at 1 A g^{-1} over 2000 cycles. In addition, a high ICE (71%) is obtained by adjusting the structure. Through a series of analyses, NPHCS demonstrates a higher ion diffusion coefficient and conductivity. This confirms that N/P dual-doping is more beneficial to improve electrochemical performance by widening the layer spacing and increasing the conductivity. Importantly, the assembled full battery also shows fine cycling stability (capacity retains 90% at 1 A g^{-1} over 300 cycles). Therefore, we propose a simple method to obtain a hard carbon for SIB anode with excellent storage performance, which is expected to be widely used in the field of energy storage.

Experimental Section

Synthesis of NPHC: Polyaniline was synthesized by an interfacial polymerization method. Typically, 2 mL phytic acid (PA, 70% in H_2O , Aladdin) was added into 20 mL deionized water, and 0.6 g ammonium persulfate (APS, 99%, Aladdin) as oxidants was also added (solution A). And 1 g aniline (99%, Aladdin) was dissolved in 30 mL toluene (99%, Guangzhou Chemical Reagent Factory) (solution B). Then, decanted solution B was into solution A at room temperature. After ten hours, the upper toluene solution was removed to obtain the product. The product was filtered and further washed with ethanol and deionized water, and then dried ($60^\circ\text{C}/12 \text{ h}$). Pyrolyzing at 800°C for 2 h in N_2 to obtain an N/P dual-doped hard carbon (NPHC) finally. For comparison, phytic acid was replaced by hydrochloric acid as the reactant. The obtained polyaniline was annealed for 2 h in N_2 at 800°C to prepare N-doped hard carbon (NHc).

Structural characterization: Field emission scanning electron microscopy (FESEM, Hitachi SU8220, Japan) was used to observe microstructures. Corresponding lattice images and energy spectrum images were obtained by high-resolution transmission electron microscopy (HRTEM, Talos F200S, America). Crystal structures were obtained by X-Ray diffraction (XRD, D8 ADVANCE Bruker, America) with $\text{Cu K}\alpha$ radiation from 10° to 70° . Raman spectroscopy (HORIBA Jobin Yvon, France) was used to characterize the internal defects. X-ray photoelectron spectroscopy (XPS, Shimadzu Axis Supra, Japan) was used to determine the chemical valence states. N_2

adsorption-desorption test (3H-2000PS1, China) was used to measure the Brunauer-Emmett-Teller (BET) specific surface area and pore size distribution.

Electrochemical measurements: First, weigh the active material, superconducting carbon black, sodium carboxymethyl cellulose three materials (mass ratio 8:1:1), and then add a certain amount of ultra-pure water for grinding. Then coated on copper foil, the amount of active material on each copper foil was controlled at 1.2 mg cm^{-2} . Finally, it was dried at 60°C for 12 hours. With metal sodium as the negative electrode, glass fiber as the diaphragm, and 1.0 M NaPF_6 in Diglyme as the electrolyte, the SIBs will be assembled in the glove box (Mikrouna) filled with argon gas. The Neware battery testing system was used to measure the galvanostatic charge/discharge curves from 0.01 to 3 V, and the CHI660E electrochemical workstation was used to analyze cyclic voltammetry (CV) and electrochemical impedance spectroscopy (EIS). Charging and discharging the SIBs to a different voltage at 0.1 A g^{-1} in the first cycle to obtain the *ex-situ* Raman spectrum. The full battery was assembled by employing the $\text{Na}_3\text{V}_2(\text{PO}_4)_2\text{F}_3$ as a cathode and NPHC as an anode. The mass ratio of the cathode to anode is 2.3:1, and the electrolyte for a full battery is 1.0 M NaPF_6 in Diglyme.

Supporting Information

Supporting Information is available from the Wiley Online Library or from the author.

Acknowledgements

This work was supported by the Guangdong University of Technology Hundred Talents Program (No. 263118136). The authors thank Dr. Wu Qiguang of GDUT Analysis and Test Center for his assistance during the TEM measurement.

Conflict of Interest

The authors declare no conflict of interest.

Data Availability Statement

The data that support the findings of this study are available from the corresponding author upon reasonable request.

Keywords: anode · hard carbon · nitrogen and phosphorus dual-doped · sodium-ion battery · synergistic effects

- [1] Z.-L. Xu, G. Yoon, K.-Y. Park, H. Park, O. Tamwattana, S. Joo Kim, W. M. Seong, K. Kang, *Nat. Commun.* **2019**, *10*, 2598.
- [2] Y. Liu, Y. Qiao, G. Wei, S. Li, Z. Lu, X. Wang, X. Lou, *Energy Storage Mater.* **2018**, *11*, 274.
- [3] X. Li, Y. Wang, L. Lv, G. Zhu, Q. Qu, H. Zheng, *Energy Mater.* **2022**, *2*, 200014.
- [4] Y. Fang, X.-Y. Yu, X. W. (David) Lou, *Adv. Mater.* **2018**, *30*, 1706668.

- [5] Z.-E. Yu, Y. Lyu, Y. Wang, S. Xu, H. Cheng, X. Mu, J. Chu, R. Chen, Y. Liu, B. Guo, *Chem. Commun.* **2020**, *56*, 778.
- [6] X. Yao, Y. Ke, W. Ren, X. Wang, F. Xiong, W. Yang, M. Qin, Q. Li, L. Mai, *Adv. Energy Mater.* **2019**, *9*, 1803260.
- [7] X. Zhao, Y. Ding, Q. Xu, X. Yu, Y. Liu, H. Shen, *Adv. Energy Mater.* **2019**, *9*, 1803648.
- [8] H. He, Q. Gan, H. Wang, G.-L. Xu, X. Zhang, D. Huang, F. Fu, Y. Tang, K. Amine, M. Shao, *Nano Energy* **2018**, *44*, 217.
- [9] B. Li, B. Xi, Z. Feng, Y. Lin, J. Liu, J. Feng, Y. Qian, S. Xiong, *Adv. Mater.* **2018**, *30*, 1705788.
- [10] L. Xu, H. Sitinamaluwa, H. Li, J. Qiu, Y. Wang, C. Yan, H. Li, S. Yuan, S. Zhang, *J. Mater. Chem. A* **2017**, *5*, 2102.
- [11] H. Jia, M. Dirican, N. Sun, C. Chen, P. Zhu, C. Yan, X. Dong, Z. Du, J. Guo, Y. Karaduman, J. Wang, F. Tang, J. Tao, X. Zhang, *Chem. Commun.* **2019**, *55*, 505.
- [12] Y. Xiao, X. Zhao, X. Wang, D. Su, S. Bai, W. Chen, S. Fang, L. Zhou, H.-M. Cheng, F. Li, *Adv. Energy Mater.* **2020**, *10*, 2000666.
- [13] G. Li, S. Guo, B. Xiang, S. Mei, Y. Zheng, X. Zhang, B. Gao, P. K. Chu, K. Huo, *Energy Mater.* **2022**, *2*, 200020.
- [14] Y. Liu, H. Dai, Y. An, L. Fu, Q. An, Y. Wu, *J. Mater. Chem. A* **2020**, *8*, 14993.
- [15] L. Chen, L. Bai, J. Yeo, T. Wei, W. Chen, Z. Fan, *ACS Appl. Mater. Interfaces* **2020**, *12*, 27499.
- [16] Y. Lu, K. H. Shin, Y. Yu, Y. Hu, J. Liang, K. Chen, H. Yuan, H. S. Park, D. Wang, *Adv. Funct. Mater.* **2021**, *31*, 2007247.
- [17] F. Wu, R. Dong, Y. Bai, Y. Li, G. Chen, Z. Wang, C. Wu, *ACS Appl. Mater. Interfaces* **2018**, *10*, 21335.
- [18] P. Wang, B. Qiao, Y. Du, Y. Li, X. Zhou, Z. Dai, J. Bao, *J. Phys. Chem. C* **2015**, *119*, 21336.
- [19] Z. Wang, W. Xu, X. Chen, Y. Peng, Y. Song, C. Lv, H. Liu, J. Sun, D. Yuan, X. Li, X. Guo, D. Yang, L. Zhang, *Adv. Funct. Mater.* **2019**, *29*, 1902875.
- [20] J. Qian, F. Wu, Y. Ye, M. Zhang, Y. Huang, Y. Xing, W. Qu, L. Li, R. Chen, *Adv. Energy Mater.* **2018**, *8*, 1703159.
- [21] Y. Zhao, F. Wang, C. Wang, S. Wang, C. Wang, Z. Zhao, L. Duan, Y. Liu, Y. Wu, W. Li, D. Zhao, *Nano Energy* **2019**, *56*, 426.
- [22] Z. Liu, L. Zhang, L. Sheng, Q. Zhou, T. Wei, J. Feng, Z. Fan, *Adv. Energy Mater.* **2018**, *8*, 1802042.
- [23] G. Zhao, D. Yu, H. Zhang, F. Sun, J. Li, L. Zhu, L. Sun, M. Yu, F. Besenbacher, Y. Sun, *Nano Energy* **2020**, *67*, 104219.
- [24] W. Nie, H. Cheng, X. Liu, Q. Sun, F. Tian, W. Yao, S. Liang, X. Lu, J. Zhou, *J. Power Sources* **2022**, *522*, 230994.
- [25] W. Li, M. Zhou, H. Li, K. Wang, S. Cheng, K. Jiang, *Energy Environ. Sci.* **2015**, *8*, 2916.
- [26] C. Li, Q. Fu, K. Zhao, Y. Wang, H. Tang, H. Li, H. Jiang, L. Chen, *Carbon* **2018**, *139*, 1117.
- [27] C. Zhou, D. Wang, A. Li, E. Pan, H. Liu, X. Chen, M. Jia, H. Song, *Chem. Eng. J.* **2020**, *380*, 122457.
- [28] W. Luo, C. Bommier, Z. Jian, X. Li, R. Carter, S. Vail, Y. Lu, J.-J. Lee, X. Ji, *ACS Appl. Mater. Interfaces* **2015**, *7*, 2626.
- [29] S. Zhong, H. Liu, D. Wei, J. Hu, H. Zhang, H. Hou, M. Peng, G. Zhang, H. Duan, *Chem. Eng. J.* **2020**, *395*, 125054.
- [30] Z. Li, Z. Jian, X. Wang, I. A. Rodríguez-Pérez, C. Bommier, X. Ji, *Chem. Commun.* **2017**, *53*, 2610.
- [31] Y. Liu, Q. Li, X. Guo, X. Kong, J. Ke, M. Chi, Q. Li, Z. Geng, J. Zeng, *Adv. Mater.* **2020**, *35*, 1907690.
- [32] H. He, D. Huang, Y. Tang, Q. Wang, X. Ji, H. Wang, Z. Guo, *Nano Energy* **2019**, *57*, 728.
- [33] J. Gao, G. Wang, W. Wang, L. Yu, B. Peng, A. El-Harairy, J. Li, G. Zhang, *ACS Nano* **2022**, *16*, 6255.
- [34] W. Wang, R. Zhang, P. Zuo, Y. Gao, G. Yin, C. Du, J. Wang, H. Huo, Y. Ma, *Energy Storage Mater.* **2021**, *37*, 199.
- [35] H. Tao, L. Xiong, S. Du, Y. Zhang, X. Yang, L. Zhang, *Carbon* **2017**, *122*, 54.
- [36] B. Sun, Q. Zhang, H. Xiang, F. Han, W. Tang, G. Yuan, Y. Cong, C. Fan, *Energy Storage Mater.* **2020**, *24*, 450.
- [37] H. Li, F. Shen, W. Luo, J. Dai, X. Han, Y. Chen, Y. Yao, H. Zhu, K. Fu, E. Hitz, L. Hu, *ACS Appl. Mater. Interfaces* **2016**, *8*, 2204.
- [38] Y. Li, B. Ni, X. Li, X. Wang, D. Zhang, Q. Zhao, J. Li, T. Lu, W. Mai, L. Pan, *Nano-Micro Lett.* **2019**, *11*, 60.
- [39] W. Shao, F. Hu, C. Song, J. Wang, C. Liu, Z. Weng, X. Jian, *J. Mater. Chem. A* **2019**, *7*, 6363.
- [40] N. Sun, Z. Guan, Y. Liu, Y. Cao, Q. Zhu, H. Liu, Z. Wang, P. Zhang, B. Xu, *Adv. Energy Mater.* **2019**, *9*, 1901351.
- [41] J. Li, L. Yu, Y. Li, G. Wang, L. Zhao, B. Peng, S. Zeng, L. Shi, G. Zhang, *Nanoscale* **2021**, *13*, 692.
- [42] H. Liu, W. Zeng, Y. Yang, J. Chen, Y. Zhao, S. Mu, *J. Mater. Chem. A* **2021**, *9*, 1260.
- [43] D. Xu, C. Chen, J. Xie, B. Zhang, L. Miao, J. Cai, Y. Huang, L. Zhang, *Adv. Energy Mater.* **2016**, *6*, 1501929.
- [44] L. Xiao, Y. Cao, W. A. Henderson, M. L. Sushko, Y. Shao, J. Xiao, W. Wang, M. H. Engelhard, Z. Nie, J. Liu, *Nano Energy* **2016**, *19*, 279.
- [45] H. Han, X. Chen, J. Qian, F. Zhong, X. Feng, W. Chen, X. Ai, H. Yang, Y. Cao, *Nanoscale* **2019**, *11*, 21999.
- [46] H. Liu, M. Jia, B. Cao, R. Chen, X. Lv, R. Tang, F. Wu, B. Xu, *J. Power Sources* **2016**, *319*, 195.
- [47] H. Hou, L. Shao, Y. Zhang, G. Zou, J. Chen, X. Ji, *Adv. Sci.* **2017**, *4*, 1600243.
- [48] X. Yuan, S. Chen, J. Li, J. Xie, G. Yan, B. Liu, X. Li, R. Li, L. Pan, W. Mai, *Carbon Energy* **2021**, *3*, 615.
- [49] Y. Zhang, Z. Zhang, Y. Tang, D. Jia, Y. Huang, Y. Guo, Z. Zhou, *J. Mater. Chem. A* **2020**, *8*, 24393.
- [50] F. Niu, J. Yang, N. Wang, D. Zhang, W. Fan, J. Yang, Y. Qian, *Adv. Funct. Mater.* **2017**, *27*, 1700522.
- [51] M. Anji Reddy, M. Helen, A. Groß, M. Fichtner, H. Euchner, *ACS Energy Lett.* **2018**, *3*, 2851.
- [52] Y.-P. Wu, C.-R. Wan, C.-Y. Jiang, S.-B. Fang, Y. Jiang, *Carbon* **1999**, *8*.
- [53] L. Shao, S. Wang, J. Qi, Z. Sun, X. Shi, Y. Shi, X. Lu, *Mater. Today Phys.* **2021**, *19*, 100422.
- [54] L. Yu, L. Shao, S. Wang, J. Guan, X. Shi, J. Cai, N. Tarasenko, Z. Sun, *Mater. Today Phys.* **2022**, *22*, 100593.

Manuscript received: September 27, 2022

Revised manuscript received: October 18, 2022

Accepted manuscript online: October 23, 2022

Version of record online: November 15, 2022